Facile preparation of $Zn_xCd_{1-x}S/ZnS$ heterostructures with enhanced photocatalytic hydrogen evolution under visible light

Jing Dong, [ID] [a] Wenjian Fang, [b] Weiwei Xia, [c] Qihong Lu [c] and Xianghua Zeng [ID] *[bc]

Hydrogen evolution from water using solar energy is regarded as a most promising process, thus, exploring efficient photocatalysts for water splitting is highly desirable. To avoid the rapid recombination of photogenerated electrons and holes in CdZnS semiconductors, $Zn_xCd_{1-x}S/ZnS$ composites were synthesized *via* a one-step hydrothermal method and then annealed at 400 °C for 60 min under argon flow. $Zn_xCd_{1-x}S/ZnS$ composites are composed of ZnS nanosheets decorated with $Zn_xCd_{1-x}S$ nanorods, and TEM and UV-vis absorption spectra confirm the formation of the heterostructure between $Zn_xCd_{1-x}S$ nanorods and ZnS nanosheets. Because of the well-matched band alignment, stronger optical absorption and larger carrier density, $Zn_{0.2}Cd_{0.8}S/ZnS$ has the highest hydrogen production, with a photocatalytic hydrogen production rate up to 16.7 mmol g^{-1} h^{-1} under visible light irradiation. Moreover, the photocatalyst also exhibits high stability and good reusability for hydrogen production reaction. The facile and efficient approach for ZnS based heterostructures could be extended to other metal compound materials.

Introduction

In consideration of the global energy crisis and environmental issues, much effort has been made to replace exhaustible fossil fuels with clean energy sources. Hydrogen, with a fuel value ($\sim$143 kJ g^{-1}) three times higher than that of gasoline and only non-polluted water as a by-product, has been regarded as one of the most important green energy carriers to replace fossil fuels. Among various strategies for hydrogen evolution, photocatalytic hydrogen evolution is regarded as the most promising way from water splitting using solar energy, because of the direct utilization of solar energy to achieve H_2 generation from water splitting, as well as its much simpler and more economically competitive systems.[1]

Ternary ZnCdS nanomaterials were regarded as a promising substitute for noble-metal co-catalysts in photocatalytic reactions because of their tunable band gap energy and lattice constant between 0.331 ($\langle 100 \rangle$ of ZnS) and 0.359 nm ($<\langle 100 \rangle$ of CdS) in comparison with ZnS or CdS materials.[2–6] Recently some studies on ZnCdS- related photocatalytic hydrogen reactions have been reported. Such as, Jin *et al.*[7] reported that ZnCdS catalysts with a (Zn + Cd) : S molar ratio of 1 : 3.5 has much higher

photocatalytic activity and exhibited an excellent stability after six cycles. And the H_2 production of (CdS–ZnS)–TiO_2 supported photocatalytic system was studied by Tambwekar *et al.*[8] The hydrogen evolution rate of ZnCdS–CdS heterostructure was obtained from 25.46 to 72.82 and 52.82 μmol h^{-1}, and the value increased to 192.28 μmol h^{-1} after the adoption of VS_2 to the heterostructure surface.[9] GQDs/ZnCdS/PdS exhibited a H_2 evolution rate of 517 μmol h^{-1}, which is 15, 7 and 1.7 times higher than that of pure ZnCdS, GQDs/ZnCdS, and ZnCdS/PdS, respectively.[10] α-Fe_2O_3/$Zn_{0.4}Cd_{0.6}S$ heterostructure has visible light photocatalytic H_2 production of 536.8 μmol h^{-1}.[11] The ZnCdS–CH solid solution without noble metal loading achieved a superior photocatalytic H_2 activity rate of 0.971 mmol h^{-1} under visible light irradiation ($\lambda \geq 420$ nm), which exceeds those of coprecipitated $Zn_{0.5}Cd_{0.5}S$ samples by more than 13 times.[12] The hydrogen production rate of $Fe_{1-x}Pt_x$-ZnCdS NPs had a significant enhancement over the pure ZnCdS (740 μmol g^{-1} h^{-1}). The hydrogen production activity of ZnCdS–NiCoP composite catalyst was improved greatly, which reached 5.2 times that of pure ZnCdS.[13] The highest hydrogen production rate of 2.265 mmol g^{-1} h^{-1} was achieved by the 0.5 wt% $Fe_{0.3}Pt_{0.7}$–ZnCdS nanocomposites, which was even better than that of 0.5 wt% Pt–ZnCdS (1.626 mmol g^{-1} h^{-1}) under the same condition.[14]

The photocatalytic H_2 evolution rate of $Zn_{0.3}Cd_{0.7}S$ nanorods was improved from 517.4 to 3310.1 μmol g^{-1} h^{-1} by loading a suitable amount of Ni_3C NPs as co-catalyst under visible light irradiation.[15] Hollow $Zn_{0.6}Cd_{0.4}S$ cage material exhibited the highest hydrogen production rate of 5.68 mmol h^{-1} g^{-1} under cocatalyst-free and visible-light irradiation conditions.[16] The

[a]College of Chemistry and Chemical Engineering, Yangzhou University, Yangzhou 225002, P. R. China

[b]College of Electrical, Energy and Power Engineering, Yangzhou University, Yangzhou 225127, P. R. China. E-mail: xhzeng@yzu.edu.cn

[c]College of Physics Science and Technology & Institute of Optoelectronic Technology, Yangzhou University, Yangzhou 225002, P. R. China

addition of NiB greatly improved the photocatalytic performance of CdZnS, and the hydrogen production of NiB/CdZnS catalysts reached 8.137 mmol g^{-1} h^{-1}, which is 17 times that of pure CdZnS.[17] A typical "type II" band alignment forms at $Zn_{0.5}Cd_{0.5}S$ hybrided with carbon materials lead to the improved H$_2$ generation rate of 10.8 mmol g^{-1} h^{-1}, exceeding the $Zn_{0.5}Cd_{0.5}S$ nanosheets (6.4 mmol g^{-1} h^{-1}) and QDs (3.4 mmol g^{-1} h^{-1}).[18] A controlled ZnCdS QDs developed by a simple ZIF-8 templating method exhibited significantly enhanced photocatalysis performance with a H$_2$ production rate of 3.70 mmol h^{-1} g^{-1} ($Zn_{0.5}Cd_{0.5}S$ QDs),[19] and the highest hydrogen production rate of $Zn_{0.5}Cd_{0.5}S$/dodecahedron ZIF-67 composite reached 23.264 mmol g^{-1} h^{-1} under visible light irradiation,[20] which was explained as the matched valence band position for ZIF-67 and ZCS and the exposure of rich active sites. The WO$_3$/ZnCdS compound catalysts showed the hydrogen production activity of the 35 wt% WO$_3$/ZnCdS to 98.68 μmol mg^{-1}, about 9.6 times that of pure ZnCdS (10.28 μmol mg^{-1}).[21]

Although many efforts have been done to develop efficient photocatalytic systems and photocatalysts by using ZnCdS materials and their composites, it is still an urgent task to develop low-cost co-catalysts for advancing photocatalytic H$_2$ production. In this paper, simple hydrothermal and annealing reaction methods were developed for preparation of pure ZnS nanosheets, CdS nanorods and $Zn_xCd_{1-x}S$/ZnS composites. The photocatalytic hydrogen production rate of $Zn_{0.2}Cd_{0.8}S$/ZnS (#3) up to 16.7 mmol g^{-1} h^{-1} has been obtained under visible light irradiation with a good stability. This value is larger than the reported pure $Zn_xCd_{1-x}S$/ZnS composites. Furthermore, the preparation method is simple. The outstanding photocatalytic performance benefited from the efficient charge transfer between ZnCdS nanorods and ZnS nanosheets in the $Zn_xCd_{1-x}S$/ZnS heterojunctions, as well as more active sites on the surface of nanosheets. This study will be helpful to obtain catalysts for photocatalytic H$_2$ production based on low-priced metal composite materials.

Experimental section

Materials and chemicals

All chemicals were analytical-grade and used without further purification. Zinc acetate [Zn(OAc)$_2$·2H$_2$O], cadmium acetate [Cd(OAc)$_2$·2H$_2$O], thiourea [(NH$_2$)$_2$CS] and ethanol were purchased from Sinopharm Chemical Reagent Co., Ltd (Shanghai China). Ethylenediamine was purchased from Aladdin Chemical Reagent Co., Ltd (Shanghai).

Sample preparation

ZnS nanosheets, CdS nanorods and $Zn_xCd_{1-x}S$/ZnS heterostructure were synthesized according to the following methods. ZnS nanosheets were prepared according to the previous reports with some modifications.[22] Typically, 60 mM Zn(OAc)$_2$·2H$_2$O was dissolved in 6 mL deionized water under constant magnetic stirring for approximately 10 min, then, 24 mL ethylenediamine was added to the solution. After the mixed solution was stirred continuously and cooled to room temperature, 0.18 M (NH$_2$)$_2$CS

was added into the above solution. After stirring for another 30 min, the mixture was transferred into a 50 mL Teflon-lined stainless steel autoclave and keeping sealed under 160 °C for 6 h. The product was collected and washed with water and ethanol for several times and dried at 60 °C for 24 h. Furthermore, the precursor was annealed in the quartz tube furnace at 400 °C for 60 min under argon (Ar) flow. After heat treatment, ZnS nanosheets were achieved, labeled as sample #1. CdS nanorods were prepared with the same procedure, except that 60 mM Cd(OAc)$_2$·2H$_2$O was used as cationic precursor (so called as sample #4). For $Zn_xCd_{1-x}S$/ZnS heterostructures, 48 mM Zn(OAc)$_2$·2H$_2$O and 12 mM Cd(OAc)$_2$·2H$_2$O were used as cationic precursor, labeled as sample #2; 36 mM Zn(OAc)$_2$·2H$_2$O and 24 mM Cd(OAc)$_2$·2H$_2$O were used as cationic precursor, named as sample #3.

Characterization

The crystal structures of the samples were analyzed by powder XRD (D8 Advance, Bruker-AXS) using Cu Kα ($\lambda = 0.154056$ nm), and their patterns were collected in the 2θ range from 10° to 80° using a continuous scanning method at a scanning speed of 2° (2θ) min^{-1}. The morphology and microstructure of the as-synthesized samples were characterized using Hitachi S-4800 field emission SEM and Tecnai G2 F30 field emission TEM, operated at an accelerating voltage of 300 kV, the composition of the products was measured by energy dispersive X-ray spectroscopy (EDX). Brunauer–Emmett–Teller (BET) surface area measurements were performed with N$_2$ adsorption at 77 K on a BSD-PS (M) instrument. Before analyses, the samples were degassed at 80 °C. Absorption measurements were carried out using a UV-vis-NIR spectrophotometer (UV-vis, Cary-5000, Varian). Photoluminescence (PL) measurements were performed using a Britain Renishaw InVia spectrophotometer, with a 325 nm line of a He–Cd laser as the excitation light source in a closed-cycle He cryostat. In addition, the chemical states of Zn, Cd and S elements were analyzed by X-ray photoelectron spectroscopy (XPS, Thermo ESCALAB250Xi) which was equipped with a standard monochromatic Al-Kα source ($h\nu = 1486.6$ eV), the binding energies were referred to C 1s peak (284.8 eV).

The PEC analysis was carried out on Zahner CIMPS electrochemical workstation (Germany) in a quartz cell, using a three-electrode cell with a Pt wire as the counter electrode, Ag/AgCl electrode as the reference electrode and FTO glass covered with photocatalyst as the working electrode. A 300 W Xe lamp (CEL-HXF 300, Beijing Au-light, China) was employed as an incident light source to study the PEC response of the samples, and Na$_2$SO$_4$ (0.2 M) solution was used as the electrolyte.

Photocatalytic H$_2$ production

The photocatalytic reactions were carried out in a Pyrex reaction cell connected to a closed gas circulation and evacuation system. Firstly, 50 mg prepared samples and H$_2$PtCl$_6$ solution (0.004 g mL^{-1}) containing 0.5 mg Pt were dispersed in 50 mL of mixed aqueous solution containing 40 mL deionized water and 10 mL sacrificial agent (lactic acid) in a Pyrex reaction cell with constant stirring. Then, the suspension was thoroughly
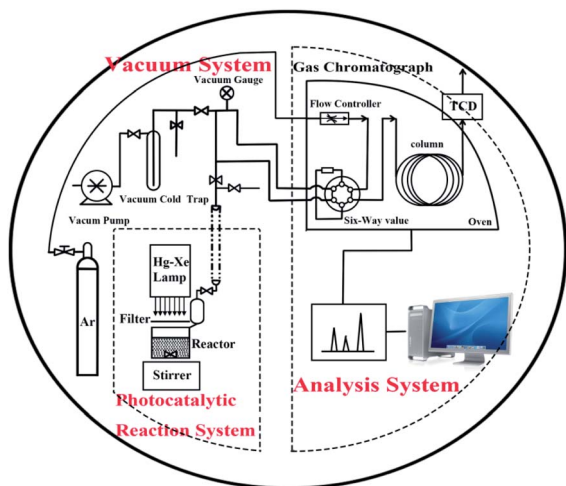
Fig. 1 Scheme of photocatalytic reactor and closed gas circulation and evacuation system made of Pyrex glass.

ZnS (PDF#36-1450) and hexagonal CdS (PDF#41-1049) for samples #1 and #4, respectively. While for samples #2 and #3, the diffraction peaks are composed with both hexagonal ZnS and hexagonal $Zn_xCd_{1-x}S$ (PDF#40-0836). With the increase of Cd precursor, the diffraction peaks belonging to $Zn_xCd_{1-x}S$ become stronger and the peak positions shift to low-angle side continuously. At the same time, the peak intensity assigned to hexagonal ZnS decreases gradually while its positions is nearly unchanged, indicating that the content of ZnS decreases constantly as shown in the magnified XRD pattern (Fig. 2b). Moreover, from the typical peak positions and Vegard's law, the lattice parameters of $Zn_xCd_{1-x}S$ solid solutions varies linearly with composition at constant temperature,[24,25] from the parameters of sample #2 and #3, we further estimate that x is approximately to 0.3 in #2, and 0.2 in #3. The main lattice parameters were displayed in Table 1. The structure and the chemical composition of sample #3 were characterized using

degassed and irradiated by a Xe lamp (300 W) with a cutoff filter (λ greater than 420 nm). The amount of H_2 was analyzed every 30 min using an online gas chromatography. The setup was designed by Liu et al.,[23] as shown in Fig. 1.

Results and discussion

The XRD patterns of the prepared samples are shown in Fig. 2a, where the diffraction peaks can be indexed as the hexagonal

Table 1 The main lattice parameters for samples #2 and #3

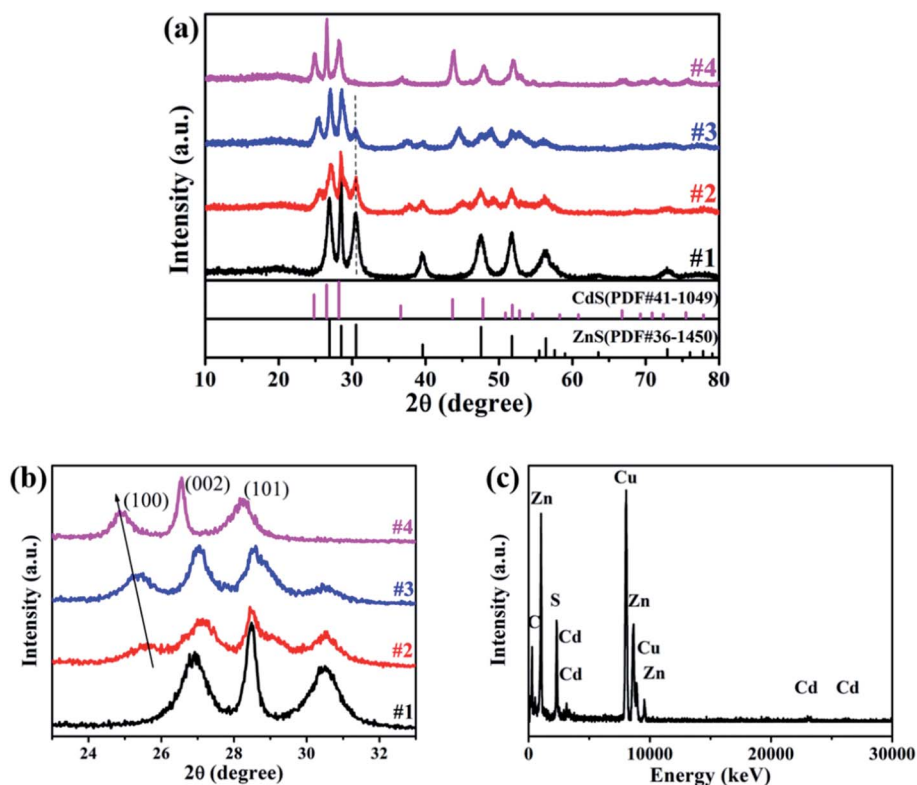|	d	$(h\ k\ l)$	2θ
#2	3.5005	(100)	25.424
	3.2940	(002)	27.047
	3.0912	(101)	28.858
#3	3.5239	(100)	25.252
	3.3105	(002)	26.910
	3.1107	(101)	28.674

Fig. 2 (a) and (b) XRD patterns of samples ZnS (#1), $Zn_xCd_{1-x}S$/ZnS (#2, #3) and CdS (#4); (c) EDX spectrum for sample #3.

Table 2 Elemental percentage in sample #3 (EDX) data

Element	Atomic percentage %
S	40.15
Zn	54.83
Cd	5.00

EDX spectroscopy, and the EDX spectrum clearly reveals the existence of Zn, Cd and Cu elements in the prepared samples, as shown in Fig. 2c.

The atomic weight percentages of the constituents are given in Table 2, we find that the metal element Zn is dominated in sample #3, and the compositional percentages of $(Zn^{2+} + Cd^{2+})$ and S^{2-} are in the required stoichiometric ratio, but larger than 1. So, there are a lots of sulfur vacancies in the prepared samples.

The morphologies of samples #1, #3 and #4 were investigated with SEM images as shown in Fig. 3. From Fig. 3a, sample #1 is composed with nanosheets, each nanosheet has a thickness of about 50 nm (inset of Fig. 3a), and sample #4 is composed with nanorods, each individual nanorod has a diameter of several tens nm and length of several hundred nm (Fig. 3b). Low- and high-magnification images of sample #3 were displayed in Fig. 3c and d, which show that after replacing Zn precursor with Cd, the products are mainly composed with nanosheets with some nanorods sparsely growing on the surface of ZnS nanosheets. Sample #2 has the same morphology as sample #3, but it is thicker and narrower than sample #3.

TEM and HRTEM measurements were carried out to investigate the microstructure features, and HAADF-STEM to determine the elements distribution. TEM images of selected

$Zn_xCd_{1-x}S/ZnS$ are displayed in Fig. 4a, the nanorods with a diameter of ~20 nm were grown on the nanosheets, which is consistent with the result of SEM. Furthermore, from the HRTEM image (Fig. 4b), one can find that the well-resolved lattice fringes with separations of 3.53 and 3.31 Å matched well with the interplanar spacing of (100) and (002) of $Zn_{0.2}Cd_{0.8}S$ with a high crystallinity, indicating that the $Zn_{0.2}Cd_{0.8}S$ nanorods grows along the [001] direction. At the same time, the lattice spacing of 3.13 Å in the nanosheet matched well with the (002) plane of hexagonal ZnS. The result is in good agreement with XRD. From elemental mappings in Fig. 4c–f, it is found that Zn and S were well-distributed, while Cd mainly gathered in nanorod area, the results confirm that #2 and #3 were composed of both ZnS nanosheets and $Zn_xCd_{1-x}S$ nanorods, and $Zn_xCd_{1-x}S$ nanorods were sparsely distributed on the surface of ZnS nanosheets.

Therefore, from the XRD patterns, SEM and TEM images show that samples #2 and #3 were composed with $ZnS/Zn_xCd_{1-x}S$ heterostructures with ZnS nanosheets decorated with $Zn_xCd_{1-x}S$ nanorods.

The PL spectra were carried out to study the properties of electrons' recombination light emission. As displayed in Fig. 5a, a wide peak from 400 to 700 nm was observed for all the samples, while ZnS (sample #1) has the strongest PL intensity, which was ascribed to the sulfur-related, zinc-related vacancies and the surface states.[26,27] A decrease in the fluorescence intensity in samples #2 and #3 implies the suppressed recombination of photogenic electron–hole pairs upon attaching $Zn_xCd_{1-x}S$ nanorods on ZnS nanosheets, and an increased photogenerated electron–hole separation, and the shift of peak position probably attributed to the transition at the interface.

UV-vis-NIR absorption spectra (Fig. 5b) reveal that samples #1 and #4 have only a single typical absorption edge, while two
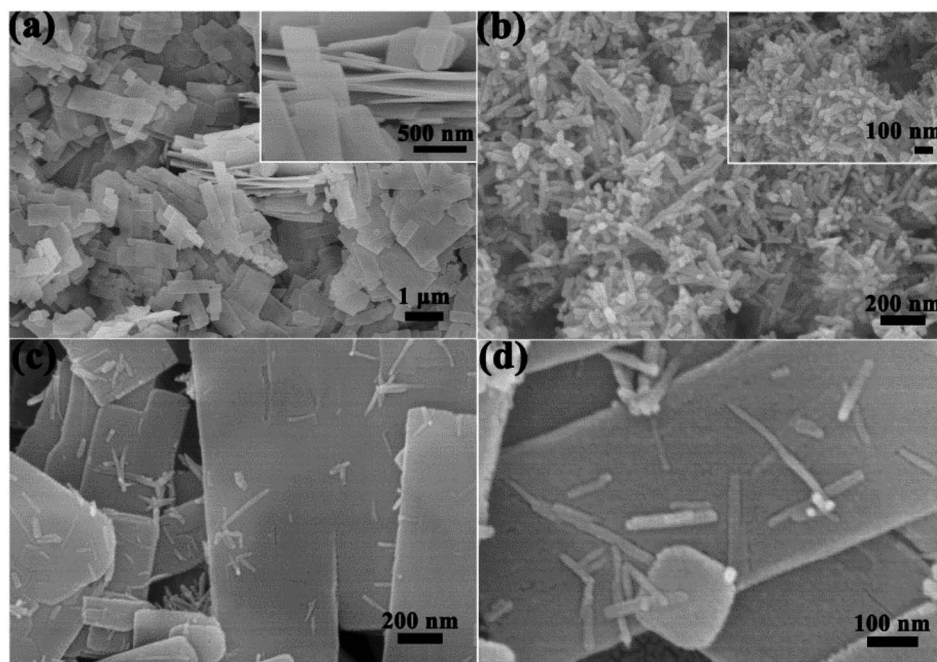

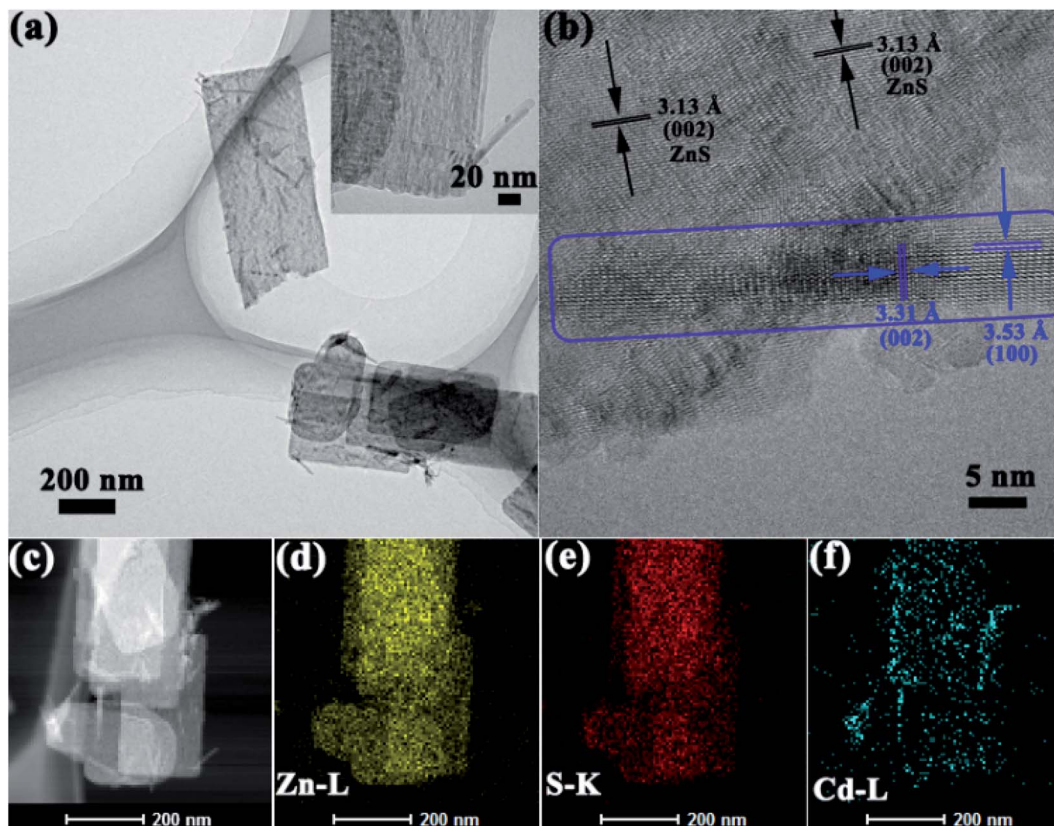**Fig. 3** SEM images of samples #1 (a), #4 (b) and #3 (c and d).

Fig. 4   (a) TEM and (b) HRTEM images, (c–f) elemental mappings of sample #3.

absorption edges can be easily found in samples #2 and #3, one at ~358 nm is ascribed to ZnS, the other at ~500 for sample #2 and ~525 nm for sample #3 can be attributed to the intrinsic bandgap absorption of $Zn_xCd_{1-x}S$. The observed two absorption edges in samples #2 and #3 reveal the formation of the Zn_x-$Cd_{1-x}S$/ZnS heterostructures. Sample #3 has a stronger absorption and bigger absorption edge than sample #2. Then, the band gap energy is obtained as 3.46, 2.48, 2.35 and 2.19 eV for samples #1–#4, respectively.

The hollow porous structures of the as-prepared samples were elucidated by nitrogen adsorption/desorption measurements to obtain their BET surface areas. As shown in Fig. 5c, the BET surface area was calculated to be 149.3 $m^2 g^{-1}$ for pure ZnS

nanosheets (#1), and 103.2, 82.3 and 20.9 $m^2 g^{-1}$ for #2, #3 and #4, respectively. From the results, one can find that pure CdS nanorods possess a low BET surface area, and sample #3 has larger BET surface than sample #2, which is favorable to adsorb molecules.

XPS measurements were used to investigate the surface composition of the four samples, the binding energies have been calibrated using the carbon C 1s peak (285.0 eV) as reference. Zn 2p spectra exhibited two peaks at ~1020.9 eV and 1043.8 eV, which were assigned to Zn $2p_{3/2}$ and $2p_{1/2}$ of Zn^{2+}, as shown in Fig. 6a. In comparison with sample #1, the Zn 2p binding energy in $Zn_xCd_{1-x}S$/ZnS heterostructures (#2, #3) has a slightly shift to higher energy, indicating the decreased

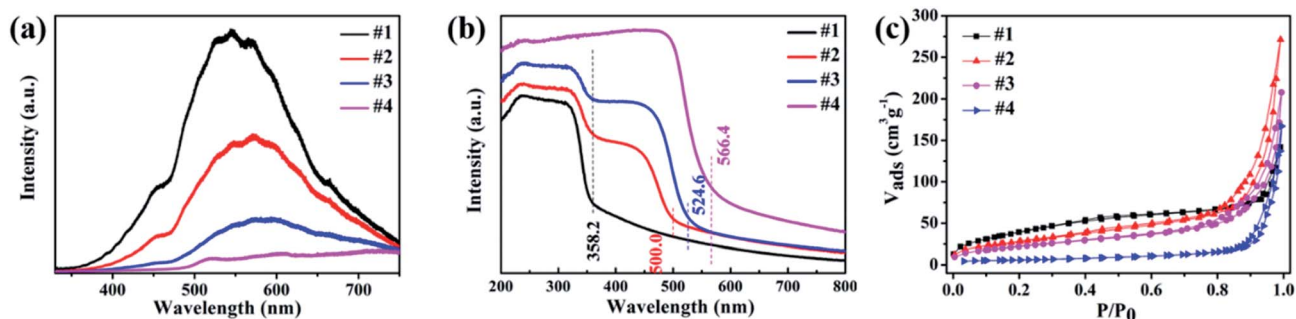

Fig. 5   (a) PL spectra, (b) UV-vis absorption spectra and (c) BET surface areas for the prepared samples ZnS (#1), $Zn_xCd_{1-x}S$ (#2, #3) and CdS (#4).
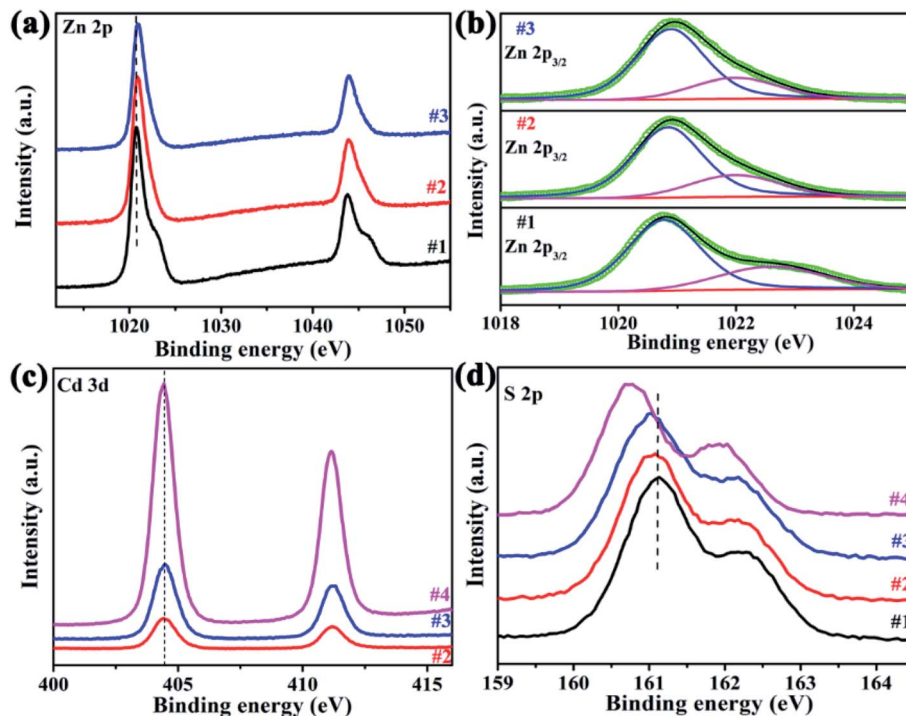
Fig. 6 XPS spectra. (a) Zn 2p, (b) deconvolved Zn 2p$_{3/2}$ peaks, (c) Cd 3d and (d) S 2p.

electron density around Zn atoms.[28] The Zn 2p$_{3/2}$ core level spectra can be deconvolved into two peaks, as shown in Fig. 6b, where the lower one is ascribed to zinc in the lattice, while the higher one was related to the Zn^{2+} in the sulfur deficient regions.[29] The relative intensity ratios between the higher one and total zinc are equal to 0.298, 0.280 and 0.285 for sample #1, #2 and #3, respectively. That means, many sulfur vacancies exist in sample #2 and #3, and the concentration is approximate,
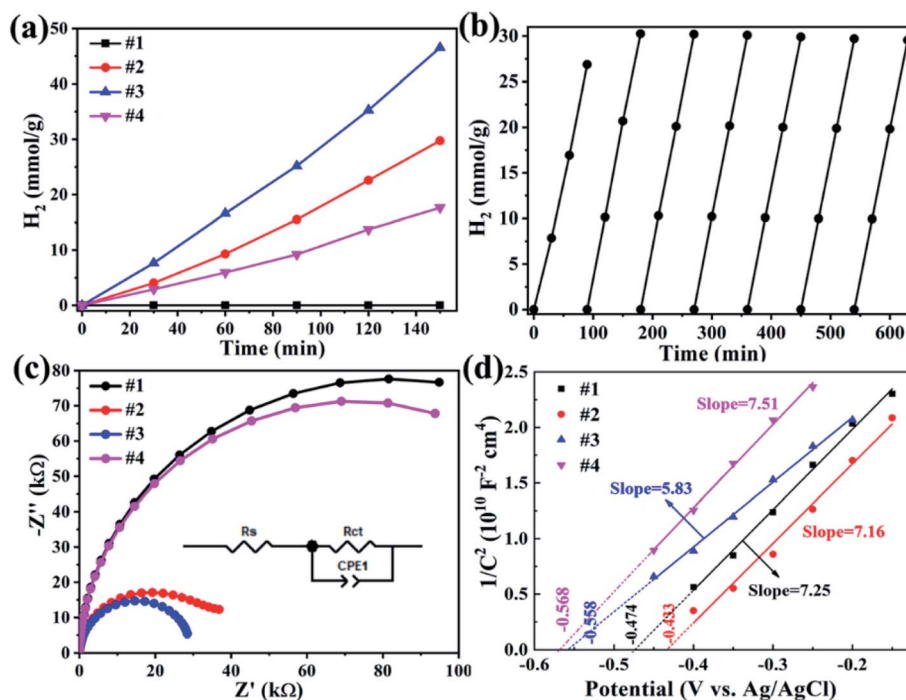

Fig. 7 (a)Hydrogen production of pure ZnS CdS and Zn$_x$Cd$_{1-x}$S/ZnS under visible light irradiation (with a 420 nm cut filter), (b) hydrogen production cycle of sample #3; electrochemical performances of all samples, (c) EIS Nyquist plots in a frequency range from 1 to 100 kHz, (d) Mott–Schottky plots at 1000 Hz.

consistent with the EDX results. The Cd 3d XPS spectra are shown in Fig. 6c, in which two peaks at 404.4 eV and 411.1 eV correspond to Cd $3d_{5/2}$ and $3d_{3/2}$, respectively, and there is no obvious peak shift between pure CdS nanorods and $Zn_xCd_{1-vx}S/ZnS$ heterostructures. For S 2p, the peaks at about 161.0 eV and 162.2 eV are belong to S $2p_{3/2}$ and S $2p_{1/2}$, as shown in Fig. 6d. With the introduction of Cd, the peaks of S shift to a lower binding energy, implying that the introduction of Cd atoms leads to the formation of $Zn_xCd_{1-x}S$. The above XPS analyses demonstrated that the electron transformation from Zn and Cd to S in $Zn_xCd_{1-x}S/ZnS$ heterostructures can increase electron density of active sites and beneficial to the various reactivity.[30,31]

The apparent quantum efficiency was measured using the 300 W xenon lamp with a 420 nm band pass filters and calculated according to eqn (1):

$$AQE(\%) = \frac{\text{number of reacted electrons}}{\text{number of incident photons}} \times 100\%$$
$$= \frac{\text{number of evolved } H_2 \text{ molecules} \times 2}{\text{number of incident photons}} 100\% \quad (1)$$

The photocatalytic H_2 production was carried out under visible light irradiation (with a 420 nm cut filter) for samples ZnS, CdS and $Zn_xCd_{1-x}S/ZnS$, as shown in Fig. 7a. From Fig. 7a, we found that pure ZnS nanosheets exhibit no photocatalytic activity due to the poor visible light absorbability, while ZnS nanosheets decorated with $Zn_xCd_{1-x}S$ nanorods reveal an enhanced photocatalytic activity. Sample $Zn_{0.3}Cd_{0.7}S/ZnS$ has a hydrogen production rate of 9.2 mmol g^{-1} h^{-1}, while $Zn_{0.2}Cd_{0.8}S/ZnS$ (#3) achieved a H_2 production rate up to 16.7 mmol g^{-1} h^{-1} with an apparent quantum efficiency of 10% at 420 nm, approximately 1.5 times of the former. The value is nearly three times of pure CdS nanorods (5.9 mmol h^{-1} g^{-1}).[32] This result is larger than recently reported 10.8 mmol g^{-1} h^{-1} with $Zn_{0.5}Cd_{0.5}S$ hybrided with carbon materials as catalysts,[18] but smaller than the value of 23.264 mmol g^{-1} h^{-1} with $Zn_{0.5}Cd_{0.5}S$/dodecahedron ZIF-67 composite.[20] Moreover, different from the reported severe photocorrosion happened in CdS materials,[33–35] the as-prepared $Zn_{0.2}Cd_{0.8}S/ZnS$ heterostructures have a relatively stable H_2 reproduction with seven consecutive cycles (Fig. 7b), and the initial low rate of hydrogen production was mainly attributed to the activation process of the catalyst.

EIS measurements was carried out to understand the charge transfer process and the electron–hole separation efficiency occurring at the interface between the photoelectrode and electrolyte, as presented in Fig. 7c, the semicircle in the Nyquist plot of each sample corresponds to the parallel combination of R_{ct} and CPE1.[36] The resultant values for the components of the EEC model corresponding to the best fit are presented in Table

3. The smaller diameter corresponds to the lower charge transfer resistance. One can find that sample #3 has smaller charge transfer resistance.

Mott–Schottky (M–S) plots were explored to determine the flatband potential (V_{fb}) for the four sample, as depicted in Fig. 7d. All curves show positive slopes, corroborating the n-type characteristics. M–S plots can also be used to estimate the electron carrier concentration using the following equation.[37]

$$N_d = \left(\frac{2}{e_0\varepsilon\varepsilon_0 A^2}\right)\left[d\left(1/C_s^2\right)/dV\right]^{-1}, \quad (2)$$

here e_0, ε and ε_0 are the electron charge with a value of 1.6×10^{19} C, dielectric constant with a value of 10,[38] and permittivity of vacuum with a value of 8.85×10^{-12} F m^{-1}, respectively. A, V and C_s are the area of the film electrode, the bias applied on the electrode and surface capacitance, respectively. From Fig. 7d, $Zn_{0.2}Cd_{0.8}S/ZnS$ (#3) has the smallest value of slope, so it has the highest carrier concentration up to 2.42×10^{19}, larger than the value of 1.95×10^{19}, 1.98×10^{19} and 1.88×10^{19} cm^{-3} for sample #1, #2 and #4, respectively. The higher carrier concentration results from the sulfur vacancy. Therefore, the enhanced H_2 production rate of sample #3 can be ascribed to the improved charge transfer activity. Besides, the flat-band potentials derived from the M–S plots are equal to -0.474, -0.433, -0.558 and -0.568 V versus Ag/AgCl electrode at neutral solution for #1, #2, #3 and #4, respectively, that correspond to the related conduction band versus Ag/AgCl electrode.[39]

In consideration of band gap energy and the conduction band potential versus Ag/AgCl electrode, the energy band alignment can be obtained for sample #3, as shown in Fig. 8. The figure shows that it is type-II heterojunction for $Zn_{0.2}Cd_{0.8}S/ZnS$ heterostructure. For $Zn_{0.2}Cd_{0.8}S/ZnS$ heterostructure, under visible-light irradiation ($\lambda > 420$ nm), electrons will be excited from the conduction band of ZnCdS nanorods to the valence band due to the lower band gap energy. As the conduction potential of ZnCdS is more negative than that of ZnS, the excited electrons will transit from the conduction band of ZnCdS nanorods to that of
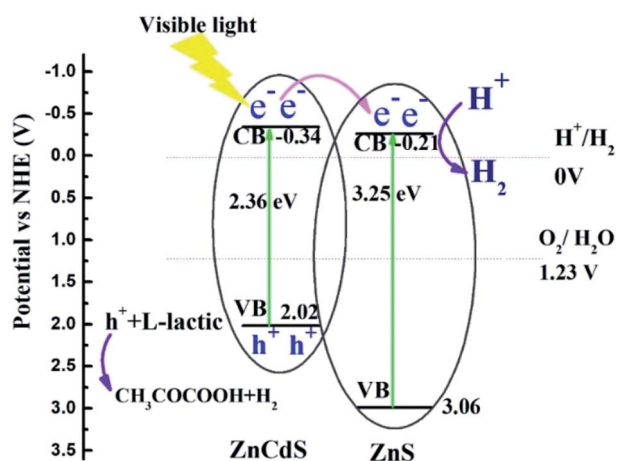

Fig. 8 The schematic illustration for electron charge transfer and H_2 evolution mechanism for the $Zn_{0.2}Cd_{0.8}S/ZnS$ nanocomposites.

Table 3 The EEC impedance parameters

Sample	#4	#1	#2	#3
R_s (kΩ)	22.31	25.32	25.83	23.16
R_{ct} (MΩ)	150.8	164.6	38.73	30.50

ZnS nanosheets, resulting in the separation of electron–hole pair. Due to the existence of internal fields, the potential barrier at the interface of the heterostructure prevents photogenerated back to ZnCdS nanorods, the photogenerated electrons have a longer lifetime. At the same time, sample #3 has higher electron carriers, meaning that the electrons could be rapidly transmitted to start reduction reaction with H_2O, producing hydrogen, while the hole sacrificial agent L-lactic acid in the system consumed electrons, forming pyruvic acid and hydrogen (h^+ + L-lactic $\rightarrow$ $CH_3COCOOH$ + H_2). These phenomena effectively promoted the photoinduced electron–hole separation and resulted in the excellent photocatalytic performance. The better photocatalytic H_2 reproduction of sample #3 than sample #2 can be ascribed to the lower charge transfer resistance and the stronger optical absorption, the lower charge transfer resistance will accelerate electrons' transition to participate the reduction reaction with H_2O; and the stronger visible light absorption of sample #3 can provide more photogenerated electrons for hydrogen production ($2H^+ + 2e^- \rightarrow H_2$).

Conclusion

In summary, pure ZnS nanosheets, CdS nanorods and Zn_x-Cd_{1-x}S/ZnS composites were synthesized *via* simple hydro-thermal and annealing reaction methods. Zn_xCd_{1-x}S/ZnS heterostructures were composed with ZnS nanosheets deco-rated with some Zn_xCd_{1-x}S nanorods. Type-II $Zn_{0.2}Cd_{0.8}$S/ZnS heterostructures have a lower charge transfer resistance, and stronger optical absorption, as well as a well-matched band energy alignment, hence they achieved a H_2 production rate up to 16.7 mmol g^{-1} h^{-1} under visible light irradiation ($\lambda > 420$ nm), approximately 1.5 and 3 times higher than that of $Zn_{0.3}Cd_{0.7}$S/ZnS (#2) and pure CdS nanorods (5.9 mmol h^{-1} g^{-1}) respectively. The strategy for the construction of hetero-junctions can provide more perspective for the preparation of photocatalyst in different application field with a simple prep-aration method.

Conflicts of interest

The authors declare no competing financial interest.

Acknowledgements

References

1 A. Fujishima and K. Honda, *Nature*, 1972, **238**, 37–38.
2 Y. Chen, X. Zhang, C. Jia, Y. Su and Q. Li, *J. Phys. Chem. C*, 2009, **113**, 2263–2266.
3 M. Yang, Y. Wang, Y. Ren, E. Liu, J. Fan and X. Hu, *J. Alloys Compd.*, 2018, **752**, 260–266.
4 A. L. Abdelhady, M. A. Malik and P. O'Brien, *J. Inorg. Organomet. Polym. Mater.*, 2014, **24**, 226–240.
5 W. Liu, H. S. Choi, J. P. Zimmer, E. Tanaka, J. V. Frangioni and M. Bawendi, *J. Am. Chem. Soc.*, 2007, **129**, 14530–14531.
6 S. Sadhu and A. Patra, *J. Phys. Chem. C*, 2012, **116**, 15167–15173.
7 Z. Jin, Y. Liu and X. Hao, *J. Colloid Interface Sci.*, 2020, **567**, 357–368.
8 S. V. Tambwekar, D. Venugopal and M. Subrahmanyam, *Int. J. Hydrogen Energy*, 1999, **24**, 957–963.
9 Y. Zhang, Y.-Z. Lin, Z.-X. Wang, K. Li, T. Li and F.-T. Liu, *Catal. Sci. Technol.*, 2019, **9**, 583–587.
10 F. Wang, Y. Su, S. Min, Y. Li, Y. Lei and J. Hou, *J. Solid State Chem.*, 2018, **260**, 23–30.
11 M. Imran, A. B. Yousaf, P. Kasak, A. Zeb and S. J. Zaidi, *J. Catal.*, 2017, **353**, 81–88.
12 C.-C. Shen, Y.-N. Liu, X. Zhou, H.-L. Guo, Z.-W. Zhao, K. Liang and A.-W. Xu, *Catal. Sci. Technol.*, 2017, **7**, 961–967.
13 H. Liu, P. Su, Z. Jin and Q. Ma, *Catal. Lett.*, 2020, **150**, 2937–2950.
14 D. Shu, H. Wang, Y. Wang, Y. Li, X. Liu, X. Chen, X. Peng, X. Wang, P. Ruterana and H. Wang, *Int. J. Hydrogen Energy*, 2017, **42**, 20888–20894.
15 Z. Luo, X. Zhao, H. Zhang and Y. Jiang, *Appl. Catal., A*, 2019, **582**, 117115.
16 J. Chen, J. Chen and Y. Li, *J. Mater. Chem. A*, 2017, **5**, 24116–24125.
17 L. Song, S. Zhang, D. Liu, S. Sun and J. Wei, *Int. J. Hydrogen Energy*, 2020, **45**, 8234–8242.
18 T. Liu, Q. Li, S. Qiu, S. Wang, X. Peng, H. Yuan and X. Wang, *Appl. Surf. Sci.*, 2020, **525**, 146586.
19 J. Chen, S. Lv, Z. Shen, P. Tian, J. Chen and Y. Li, *ACS Sustainable Chem. Eng.*, 2019, **7**, 13805–13814.
20 H. Gong, X. Zhang, G. Wang, Y. Liu, Y. Li and Z. Jin, *Mol. Catal.*, 2020, **485**, 110832.
21 L. Song, D. Liu, S. Zhang and J. Wei, *Int. J. Hydrogen Energy*, 2019, **44**, 16327–16335.
22 W. Feng, Y. Wang, X. Huang, K. Wang, F. Gao, Y. Zhao, B. Wang, L. Zhang and P. Liu, *Appl. Catal., B*, 2018, **220**, 324–336.
23 H. Liu, J. Yuan, Z. Jiang, W. Shangguan, H. Einaga and Y. Teraoka, *J. Mater. Chem.*, 2011, **21**, 16735–16743.
24 X. Zhong, Y. Feng, W. Knoll and M. Han, *J. Am. Chem. Soc.*, 2003, **125**, 13559–13563.
25 J. Xu, X. Yang, H. K. Wang, X. Chen, C. Y. Luan, Z. X. Xu, Z. Z. Lu, V. A. L. Roy, W. J. Zhang and C. S. Lee, *Nano Lett.*, 2011, **11**, 4138–4143.
26 B. Poornaprakash, D. A. Reddy, G. Murali, N. M. Rao, R. P. Vijayalakshmi and B. K. Reddy, *J. Alloys Compd.*, 2013, **577**, 79–85.
27 J. Dong, X. H. Zeng, W. W. Xia, X. Y. Zhang, M. Zhou and C. X. Wang, *RSC Adv.*, 2017, **7**, 20874–20881.
28 Q. Zhu, Z. Xu, Q. Yi, M. Nasir, M. Xing, B. Qiu and J. Zhang, *Mater. Chem. Front.*, 2020, **4**, 3234–3239.
29 X. Gu, S. Zhang, Y. Zhao and Y. Qiang, *Vacuum*, 2015, **122**, 6–11.
30 X.-L. Yin, G.-Y. He, B. Sun, W.-J. Jiang, D.-J. Xue, A.-D. Xia, L.-J. Wan and J.-S. Hu, *Nano Energy*, 2016, **28**, 319–329.

31 B. Ma, P.-Y. Guan, Q.-Y. Li, M. Zhang and S.-Q. Zang, *ACS Appl. Mater. Interfaces*, 2016, **8**, 26794–26800.

32 D. Huang, M. Wen, C. Zhou, Z. Li, M. Cheng, S. Chen, W. Xue, L. Lei, Y. Yang, W. Xiong and W. Wang, *Appl. Catal., B*, 2020, **267**, 118651.

33 P. Wang, H. T. Li, Y. Sheng and F. Chen, *Appl. Surf. Sci.*, 2019, **463**, 27–33.

34 Y. Y. Zhong, G. Zhao, F. K. Ma, Y. Z. Wu and X. P. Hao, *Appl. Catal., B*, 2016, **199**, 466–472.

35 H. G. Yu, X. Huang, P. Wang and J. G. Yu, *J. Phys. Chem. C*, 2016, **120**, 3722–3730.

36 Z. Seidalilir, E. Soheyli, M. Sabaeian and R. Sahraei, *J. Mol. Liq.*, 2020, **320**, 114373.

37 X. Zhao, J. Feng, S. Chen, Y. Huang, T. C. Sum and Z. Chen, *Phys. Chem. Chem. Phys.*, 2017, **19**, 1074–1082.

38 I. Cesar, K. Sivula, A. Kay, R. Zboril and M. Graetzel, *J. Phys. Chem. C*, 2009, **113**, 772–782.

39 S. S. Yi, J. M. Yan, B. R. Wulan, S. J. Li, K. H. Liu and Q. Jiang, *Appl. Catal., B*, 2017, **200**, 477–483.